Implementing recyclable bio- and CO_2-sourced synergetic dynamic matrices via precise control of curing and properties for natural fiber composites within industrially relevant resin transfer molding

Guillem Seychal*[1,2], Bernard Miranda Campos[3], Gabriel Perli[1], Vincent Placet[4], Bruno Grignard[5], Fanny Bonnet†[3], Christophe Detrembleur[5,6], Haritz Sardon[1], Nora Aranburu‡[1], and Jean-Marie Raquez§[2,6]

[1] *POLYMAT and Department of Advanced Polymers and Materials: Physics, Chemistry, and Technology, Faculty of Chemistry, University of the Basque Country UPV/EHU, Paseo Manuel de Lardizabal 3, Donostia-San Sebastián, 20018, Spain*

[2] *Laboratory of Polymeric and Composite Materials, Center of Innovation and Research in Materials and Polymers (CIRMAP), University of Mons, Place du Parc 23, Mons, 7000, Belgium*

[3] *Univ. Lille, CNRS, INRAE, Centrale Lille, UMR 8207 - UMET - Unité Matériaux et Transformations, F-59000 Lille, France*

[4] *Université de Franche-Comté, SUPMICROTECH-ENSMM, CNRS, Institut FEMTO-ST, 25000, Besançon, France*

[5] *Department of Chemistry, Center for Education and Research on Macromolecules (CERM), University of Liège, Sart-Tilman, B6A, Liège, 4000, Belgium*

[6] *WEL Research Institute, Wavre 1300, Belgium*

Supplementary Informations

Contents

*guillem.seychal@umons.ac.be
†fanny.bonnet@univ-lille.fr
‡nora.aramburu@ehu.eus
§jean-marie.raquez@umons.ac.be

List of Figures

I Chemical synthesis of model and building blocks

I.1 Butyl Carbonate

Butyl Carbonate (BGC) was synthesized through the direct carbonatation of butyl glycidyl ether (BGE). 25 g of BGE was introduced in a 100 mL high-pressure stainless steel reactor with 2.5 mol% (vs BGE) of TBAI as the catalyst. The reactor was closed and stabilized at 80 °C and 110 bar of CO_2 pressure for 24 h. The crude was collected, degassed under vacuum, dissolved in ethyl acetate, and washed two times with distilled water and once with brine to remove the catalyst. The obtained product was characterized by ^{1}H-NMR (Fig. S1).

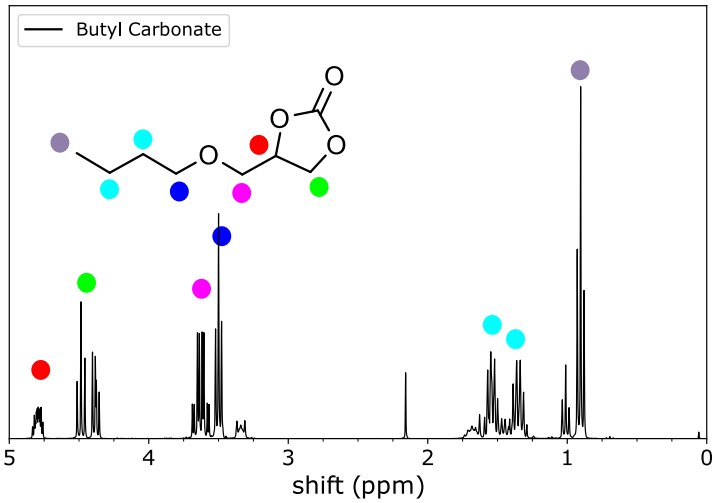

Figure S1: ^{1}H-NMR in $CDCl_3$ of the butyl carbonate compound

I.2 Trimethylolpropane tricarbonate

Trimethylolpropane tricarbonate(TMPTC, Carbonate Equivalent Weight CEW = 175 g/eq) was synthesized in a large scale from its respective epoxide precursor as described in a previous study [1]. Shortly, about 25 kg of TMPTGE were introduced in a 50 L high-pressure stainless steel reactor with 2.5 mol% (vs TMPTGE) of TBAI as the catalyst. The reactor was closed and stabilized at 80 °C and 110 bar of CO_2 pressure for 24 h. The crude was collected, degassed under vacuum, and used without any purification. The obtained product was characterized by ^{1}H-NMR (Fig. S2.

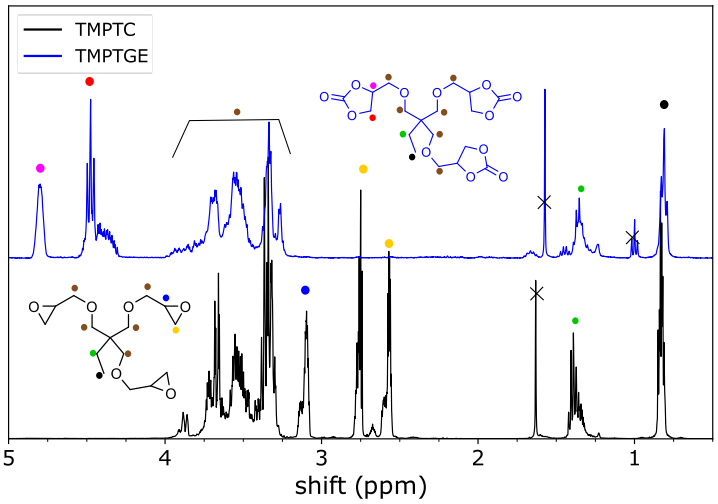

Figure S2: ^{1}H-NMR in $CDCl_3$ of the epoxy precursor (TMPTGE) and the resulting carbonate (TMPTC)

I.3 2-Hydroxyethyl n-butylcarbamate

2-Hydroxyethyl n-butylcarbamate (mHU) was synthesized in a 25 mL round bottom flask. Ethylene carbonate (EC, 1 eq) was mixed with n-butylamine (1.1 eq) and reacted at 60 °C for 24 h under constant stirring. The crude was then dissolved in methanol and filtered through a short acidic silica column to eliminate the excess amine. Methanol was then eliminated using a rotary evaporator. The obtained product was characterized by ^{1}H-NMR (Fig. S3).

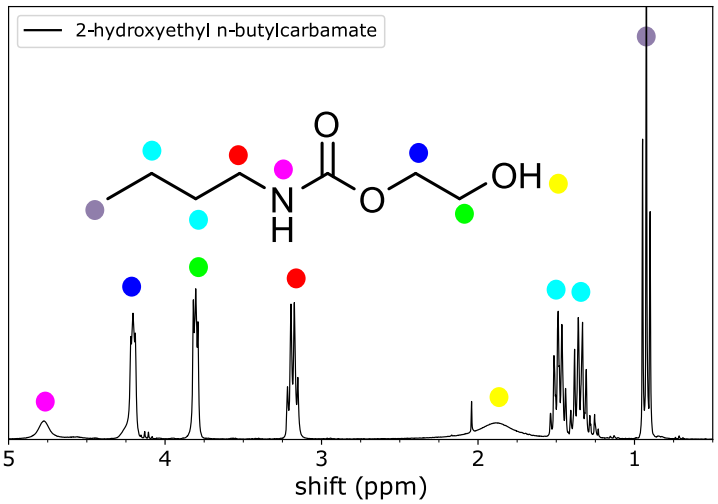

Figure S3: ^{1}H-NMR in $CDCl_3$ of the 2-Hydroxyethyl n-butylcarbamate (mHU) model compound

I.4 Ethyl n-propylcarbamate

Ethyl n-propylcarbamate (mU) was synthesized in a 25 mL round bottom flask. In a large excess of dry ethanol (10 eq) under constant stirring, propyl isocyanate (1 eq) was added dropwise and left to stir at room temperature for 1 h. The excess ethanol was then removed by vacuum evaporation. No further purification was conducted. The obtained product was characterized by ^{1}H-NMR (Fig. S4).

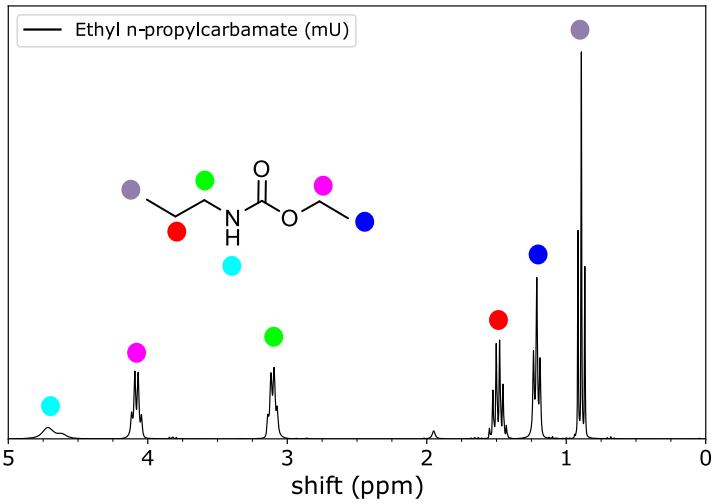

Figure S4: ^{1}H-NMR in $CDCl_3$ of the ethyl n-propylcarbamate (mU) model compound

I.5 1-Benzylamino-3-butoxy-propan-2-ol

1-Benzylamino-3-butoxy-propan-2-ol (mEP) was synthesized by mixing BGE (1eq) with n-butylamine (1.1 eq) in a 25 mL round bottom flask and reacted at 60 °C for 24 h under constant stirring. The crude was then dissolved in methanol and filtered through a short acidic silica column to eliminate the amine excess. Methanol was then removed using a rotary evaporator. The obtained product was characterized by ^{1}H-NMR (Fig.S5).

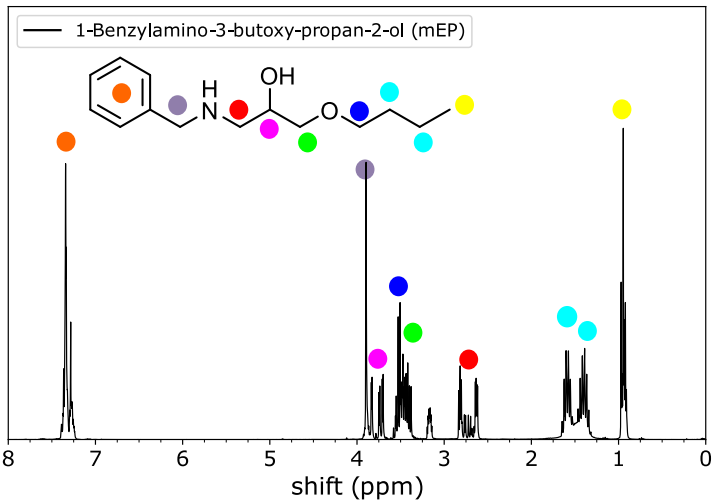

Figure S5: ^{1}H-NMR in $CDCl_3$ of the 1-Benzylamino-3-butoxy-propan-2-ol (mEP) model compound

II Characterisation

II.1 H-NMR spectroscopy

^{1}H-NMR were performed on a Bruker Advance 300 (300 MHz) spectrometer using deuterated chloroform ($CDCl_3$) as solvent at ambient temperature (298 K).

II.2 Fourier-transform infrared spectroscopy (FTIR)

A Bruker FTIR Tensor 27 spectrometer was employed for FTIR in attenuated total reflectance mode with a 4 cm^{-1} resolution over 4000–600 cm^{-1} range.

II.3 Matrix curing analyses through differential scanning calorimetry (DSC), isothermal rheometry, and Friedman's model

The formulations' curing behavior was investigated first by DSC using a TA instruments Discovery 25 apparatus with aluminum hermetic pans. About 5 mg of the uncured system was precisely weighed. Non-isothermal curing analyses were performed from 25 °C to 220 °C at 5,10, and 20 °C/min heating rates. Isothermal curing was performed at 80 °C for 1 hour with a 10 °C/min heating ramp to reach the targeted temperature. The conversion degree can be computed through the ratio between partial enthalpy and the total enthalpy as described in eq.1. The non-isothermal DSC measurements were used to evaluate the activation energy (E_a) in the n^{th} order kinetic model [2, 3] described in eq. 2 of the systems using Friedman's model (eq.3).

$$\alpha = \frac{\int_{t_0}^{t} H_t}{\Delta H_T} \tag{1}$$

$$\frac{d\alpha}{dt} = Ae^{-\frac{E_a}{RT}}(1-\alpha)^n \tag{2}$$

$$\ln\frac{d\alpha}{dt} = \ln Af(\alpha) - \frac{E_a}{RT} \tag{3}$$

where α is the curing advance, H_T is the curing enthalpy, R is the perfect gas constant, and A the pre-exponential factor.

The curing of unreacted matrix formulations was also measured by rheology. Isothermal measurements at 25 and 80 °C were performed on an Anton Paar Rheometer MCR302 with 1 mm separated parallel aluminum plates (25 mm diameter). Per measurements, 1.0 g of product was used. A 2% strain was applied at 1 Hz.

II.4 Fiber volume fraction and porosities

The fiber mass was calculated using eq.(4). Fiber volume fraction (V_f) was calculated using eq.(5) and void content (V_v) was calculated using eq.(6).

$$m_f = n \times A_r \times S \tag{4}$$

$$V_f = \frac{\frac{m_f}{\rho_f}}{\frac{m_f}{\rho_f} + \frac{m_c - m_f}{\rho_m}} \tag{5}$$

$$V_v = 1 - \rho_c\left(\frac{w_m}{\rho_m} + \frac{w_f}{\rho_f}\right) \tag{6}$$

in which n is the plies quantity, S is the sample's cross-section area, and A_r is the flax tape areal weight. ρ_x, m_x, and w_x refer to the density, the mass, and the weight fraction respectively. f subscript refers to fibers, m to the matrix, and c to the composite. Flax' density was chosen from the supplier technical data sheet at 1.45 g/cm^3. Matrix density values were measured in ethanol using Archimedes's principle.

II.5 Dynamical mechanical analysis (DMA)

DMA in tension was conducted on a TA Instruments DMAQ800 from 25 °C to 160 °C at a 3 °C/min heating rate, and a 0.1% strain was applied at 1 Hz. Rectangular samples of 20x8x0.8 mm^3 were employed with a gauge length of 10 mm. The crosslinking density ($\nu_{E'}$) was determined using eq. (7)

$$\nu_{E'} = \frac{E'_{T_{\alpha+50}}}{3RT_{\alpha+50}} \quad (7)$$

where $T_{\alpha+50}$ is the temperature, taken 50 K after the α transition, $E'_{T_{\alpha+50}}$ the storage modulus at $T_{\alpha+50}$.

II.6 Characterization of materials mechanical properties

Before all tests, a conditioning for at least 48 h at 23 °C under a relative humidity of 50 ± 5% was applied. The values were averaged over five measurements. Monotonic tensile testing at a 1 mm/min displacement rate (ASTM D638) of type V dog-bone shape matrices was performed on a ZwickRoell Z2.5 using a 2.5 kN cell force. Linear regression between 0.1% and 1.0% strain in the elastic region was done to compute the elastic modulus.

The three-point monotonic bending properties of composites (ASTM D790) were performed on the two main orthotropic directions of the materials. A span length of 32 mm was used, and a 0.1 MPa preload applied to guarantee full contact. Rectangular samples of 50.8x12.7x1.2 mm^3 geometry were tested at 1 mm/min. The bending modulus (E) was calculated between 0.1 and 0.5% bending strain.

Flatwise Charpy unnotched impact tests were carried out on a Ray-Ran 2500 pendulum impact tester. A hammer of 0.668 kg with a 3.46 m/s impact speed was used to apply 2.71 J impact energy.

II.7 ThermoGravimetric Analysis (TGA)

For TGA measures, about 10 mg of product was analyzed in a TA Q500. The analysis was conducted at 20 °C/min under a 60 mL/min N_2 flow from 25 to 800 °C.

II.8 X-ray photoelectron spectroscopy (XPS)

XPS measurements were performed on a Versaprobe III Physical Electronics (ULVAC) system with a monochromatic Al Kα radiation source (1486.7 eV). An initial analysis was carried out to determine the elements present (wide scan: step energy 0.2 eV, pass energy 224 eV) and detailed analyses were carried out on the detected elements (detail scan: step energy 0.05 eV, pass energy 27 eV, time per step 20 ms) with an electron exit angle of 45º. The spectrometer was previously calibrated with Ag (Ag 3d5/2, 368.26 eV). The spectra were fitted using the CasaXPS 2.3.26 software, which models the contributions after a background subtraction (Shirley).

II.9 Tensile testing of the flax yarns

The tensile testing of virgin and recovered flax yarns was performed using a capstan system (Fig. S6) to guarantee systematic failure within the span length. A 70 mm span length was used. The test speed was set to 1 mm/min. A 1 kN cell was used on a MTS Criterion 45 tensile machine.

Figure S6: Flax yarn tensile testing capstan set-up.

II.10 Theoretical bending modulus of the laminates

To allow the comparison of the present work with the literature, the classical laminate theory (CLT) was used to predict the properties of each laminate. Chamis' micromechanical model [4] was used first to predict the local properties of a single ply using eq.(8) and eq.(9) for the longitudinal and transverse modulus, respectively. Poisson ratio were calculated from eq. (10) and (11). Matrix properties were taken from the present study (subscript m), the Poisson ratio was set to 0.4. The reinforcement properties (subscript f) were back-calculated from the technical datasheet of the supplier (E_{11_f} = 35 GPa, E_{22_f} = 8 GPa, ν = 0.49).

$$E_1 = V_f E_{11_f} + (1 - V_f) E_m \tag{8}$$

$$E_2 = \frac{E_m}{1 - \sqrt{V_f}(1 - E_m / E_{22_f})} \tag{9}$$

$$\nu_{12} = V_f \nu_f + V_m \nu_m \tag{10}$$

$$\nu_{21} = \nu_{12} \frac{E_2}{E_1} \tag{11}$$

From Chami's modulus, the stiffness matrix Q is calculated in the ply local coordinates.

$$Q = \begin{bmatrix} Q_{11} & Q_{12} & 0 \\ Q_{12} & Q_{22} & 0 \\ 0 & 0 & G_{66} \end{bmatrix} \tag{12}$$

$$Q_{11} = \frac{E_1}{1 - \nu_{12}\nu_{21}} \tag{13}$$

$$Q_{22} = \frac{E_2}{1 - \nu_{12}\nu_{21}} \tag{14}$$

$$Q_{12} = \frac{\nu_{12}E_2}{1 - \nu_{12}\nu_{21}} \tag{15}$$

$$G_{66} = 0 \tag{16}$$

Each ply stiffness is then calculated in the global coordinates, following eq.(17).

$$Q' = T^{-1}QT \tag{17}$$

where T is the transformation matrix from the ply orientation angle θ.

$$T = \begin{bmatrix} m^2 & n^2 & 2mn \\ n^2 & m^2 & -2mn \\ -mn & mn & m^2 - n^2 \end{bmatrix} \tag{18}$$

with m = cosθ, and n = sinθ.

The equivalent bending stiffness matrix [D] is then calculated as follows:

$$D = \frac{1}{3}\sum_{n=1}^{N} Q'(z_k^3 - z_{k-1}^3) \tag{19}$$

with z_k being the z coordinates of the ply k from the middle axis of the laminate.

from [D], the theoretical bending modulus can be obtained:

$$E_{B_1} = D_{11}\frac{12}{h^3} \tag{20}$$

$$E_{B_2} = D_{22}\frac{12}{h^3} \tag{21}$$

with h the total thickness of the laminate.

III Mutual catalytic effect on the aminolysis of CC and epoxy compounds

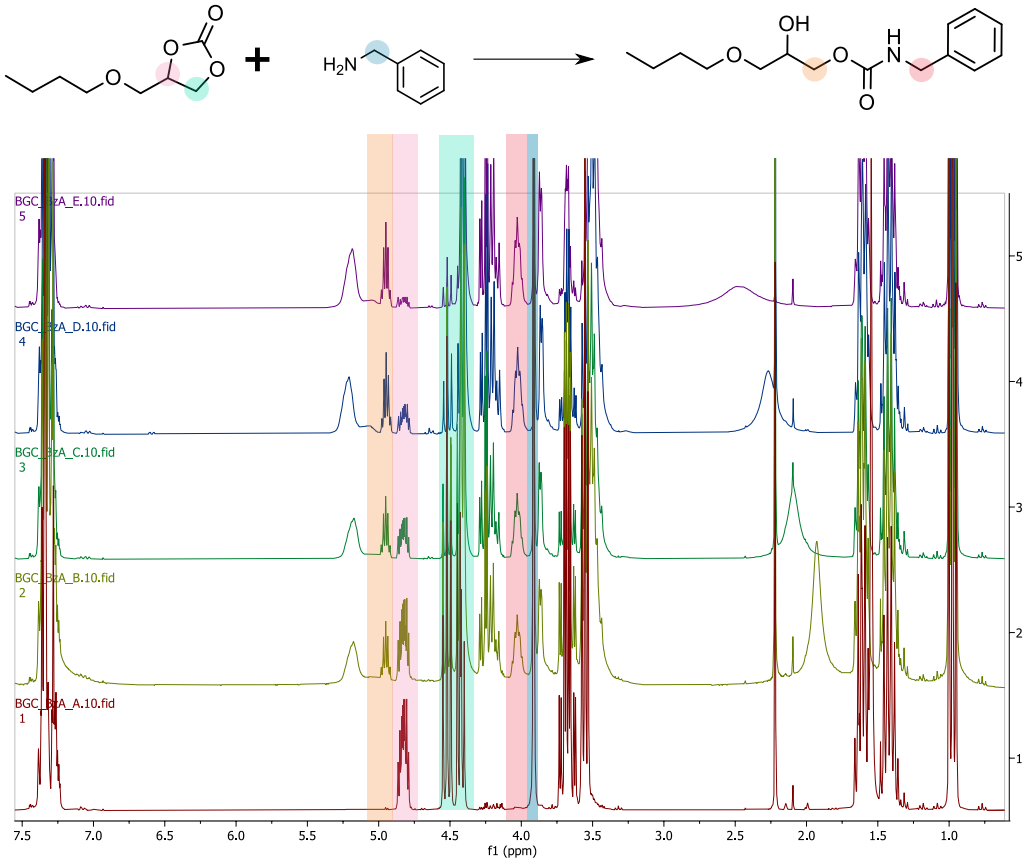

Figure S7: ^{1}H-NMR kinetic model reaction in $CDCl_3$. Aminolysis of butyl carbonate by benzylamine.

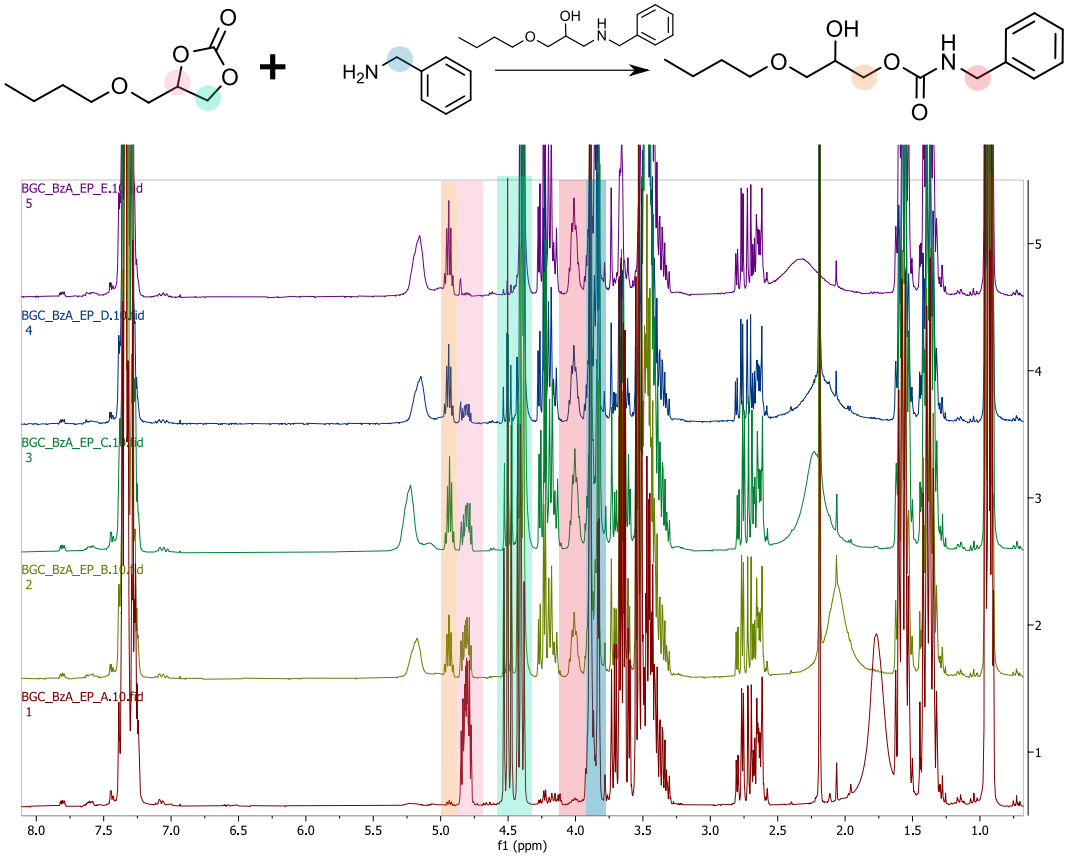

Figure S8: ^{1}H-NMR kinetic model reaction in $CDCl_3$. Aminolysis of butyl carbonate by benzylamine in the presence of epoxy model compound (0.5eq mEP).

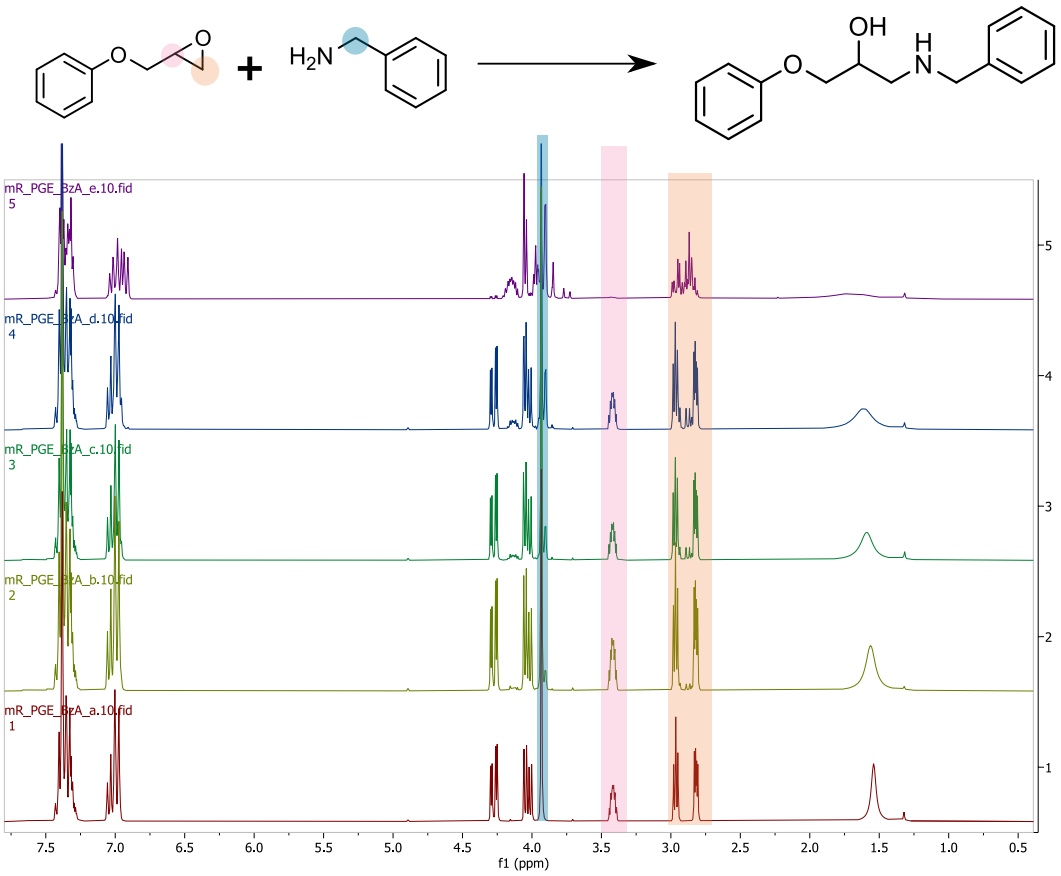

Figure S9: ^{1}H-NMR kinetic model reaction in $CDCl_3$. Aminolysis of phenyl glycidyl ether by benzylamine.

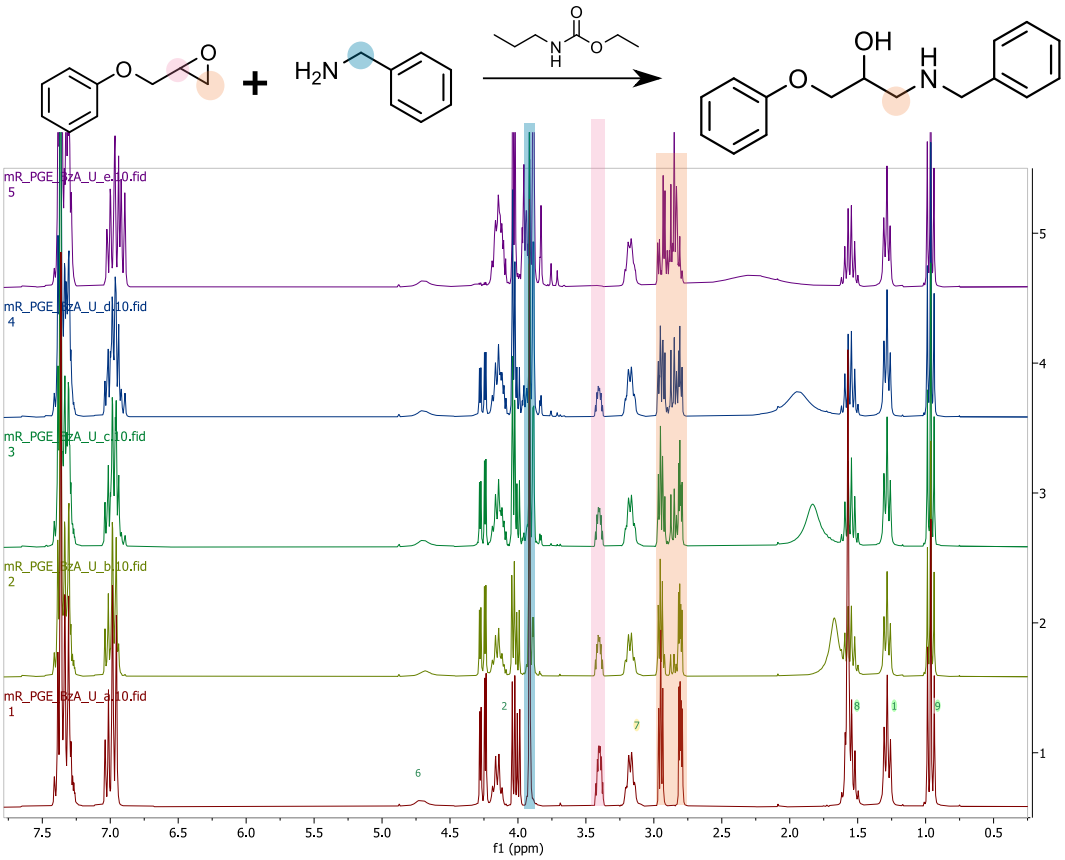

Figure S10: ^{1}H-NMR kinetic model reaction in $CDCl_3$. Aminolysis of phenyl glycidyl ether by benzylamine in the presence of model urethane compound (mU, 0.5eq).

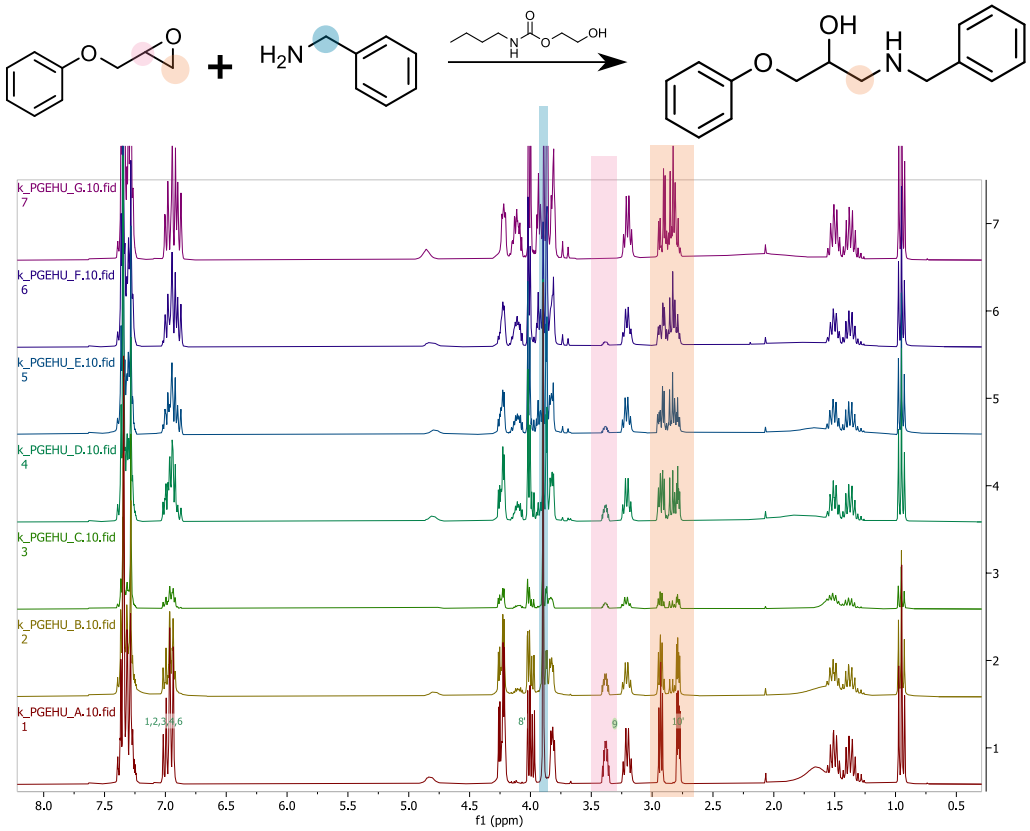

Figure S11: ^{1}H-NMR kinetic model reaction in $CDCl_3$. Aminolysis of phenyl glycidyl ether by benzylamine in the presence of model hydroxyurethane compound (mHU, 0.5eq).

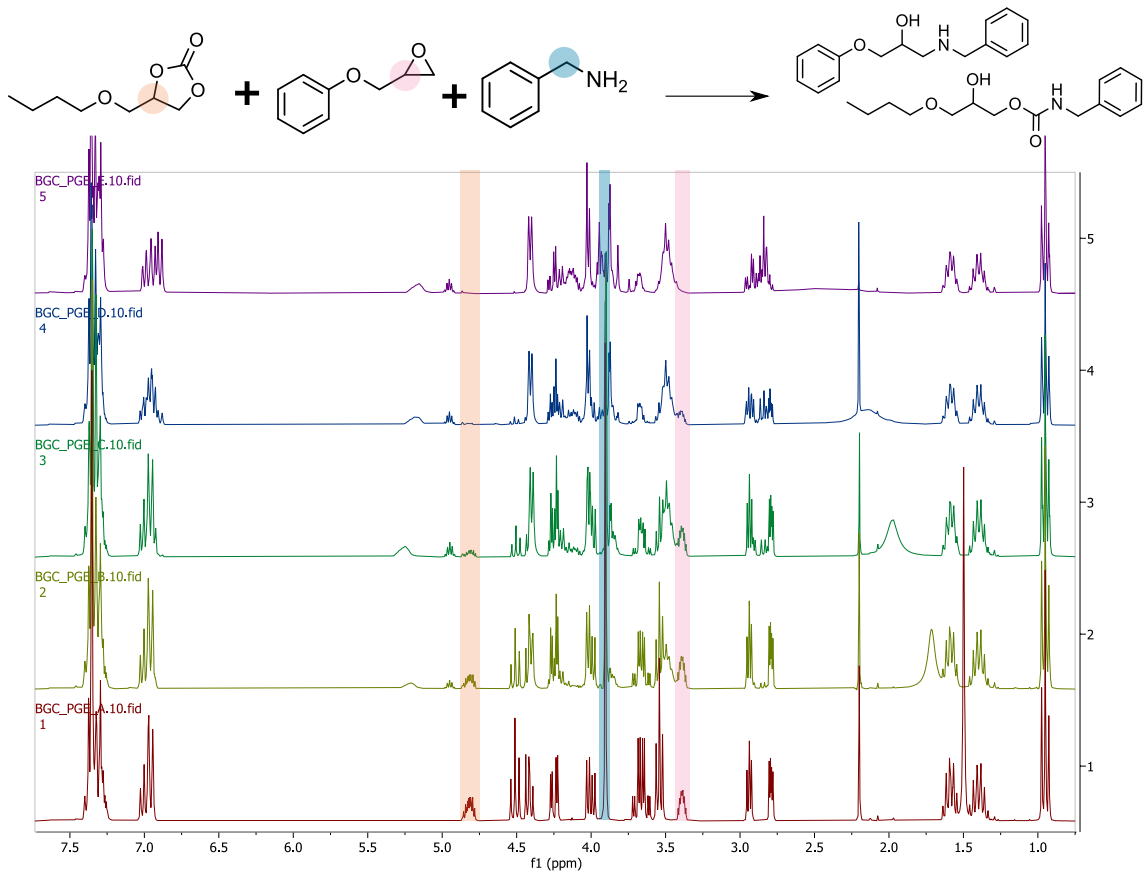

Figure S12: ^{1}H-NMR kinetic model reaction in $CDCl_3$. Simultaneous aminolysis of phenyl glycidyl ether and butyl carbonate by benzylamine.

IV Curing behavior of hybrid EP-CC through DSC and rheology

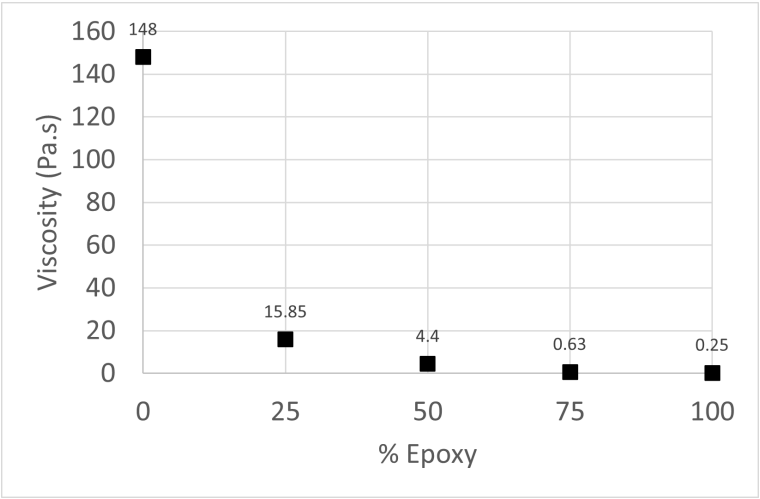

Figure S13: Viscosity of the EP-CC mixture (prior to addition of amine hardener).

IV.1 Non-Isothermal DSC

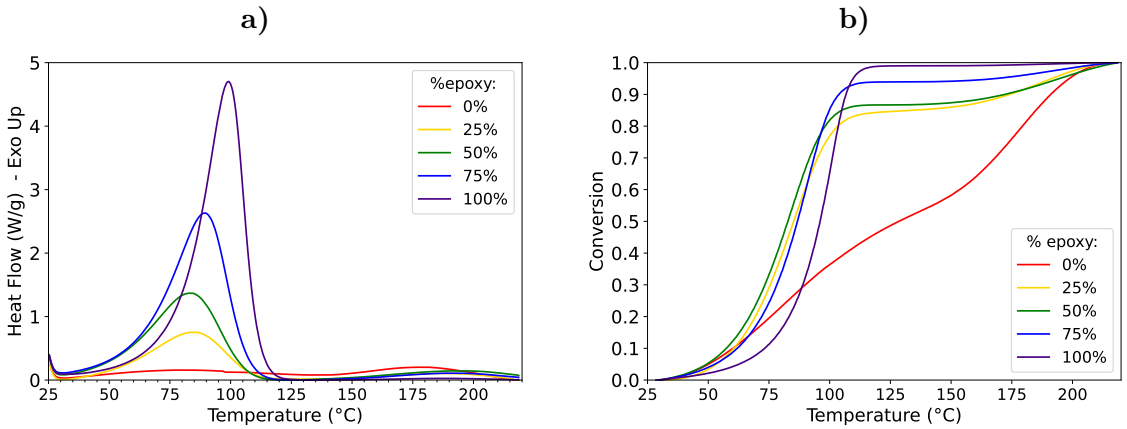

Figure S14: Non-Isothermal DSC at 10 K/min. a) Thermograms, and b) advance curing.

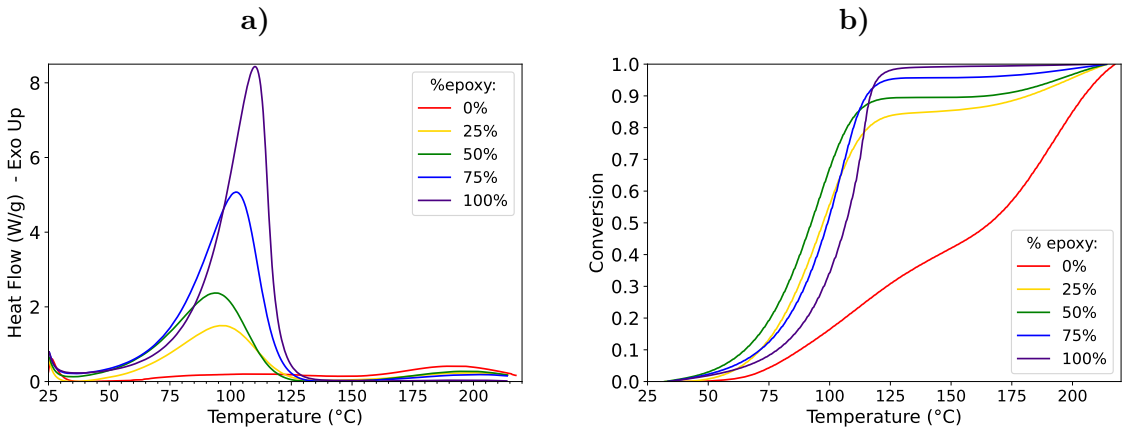

Figure S15: Non-Isothermal DSC at 20 K/min. a) Thermograms, and b) advance curing.

IV.2 Friedman's Isoconversional plot

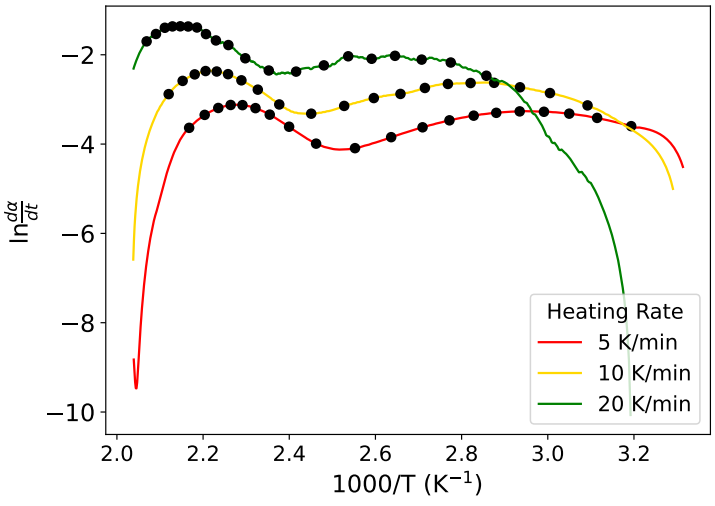

Figure S16: Friedman's Isoconversional plot for the PHU (0% EP)

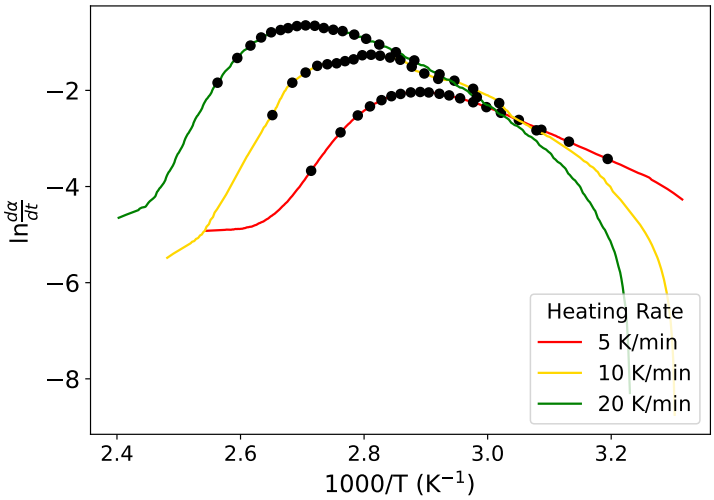

Figure S17: Friedman's Isoconversional plot for the hybrid EP-CC (25% EP)

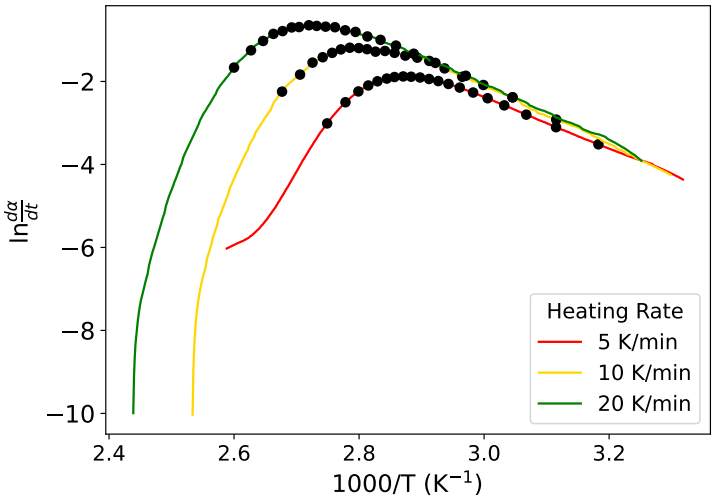

Figure S18: Friedman's Isoconversional plot for the hybrid EP-CC (50% EP)

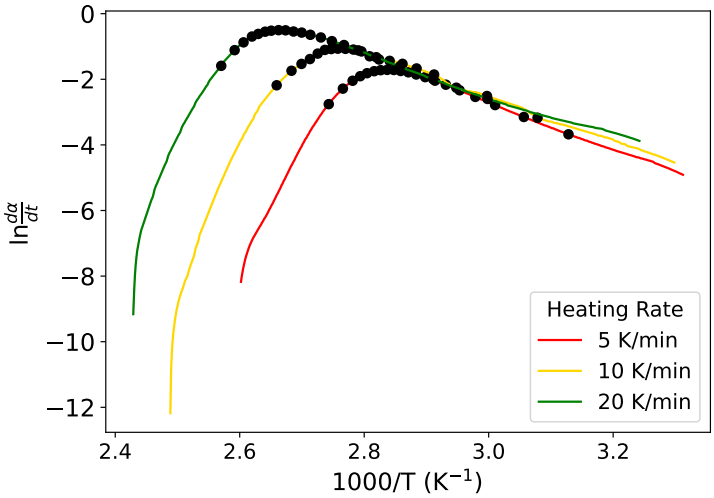

Figure S19: Friedman's Isoconversional plot for the hybrid EP-CC (75% EP)

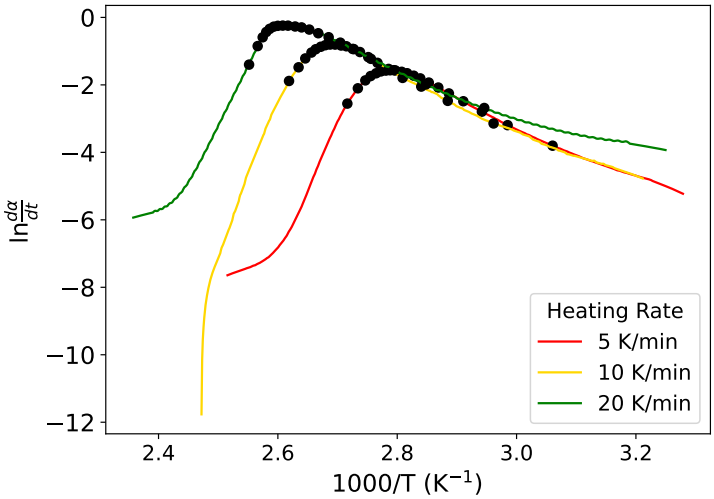

Figure S20: Friedman's Isoconversional plot for the epoxy resin(100% EP)

IV.3 Rheological supplementary informations

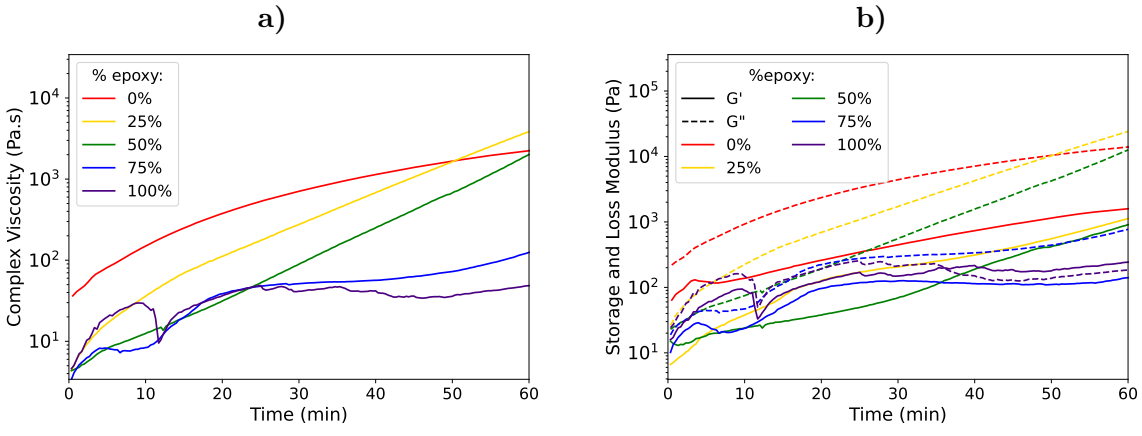

Figure S21: Curing rheological behavior at 25°C. a) Viscosity Evolution, and b) Modulus plot.

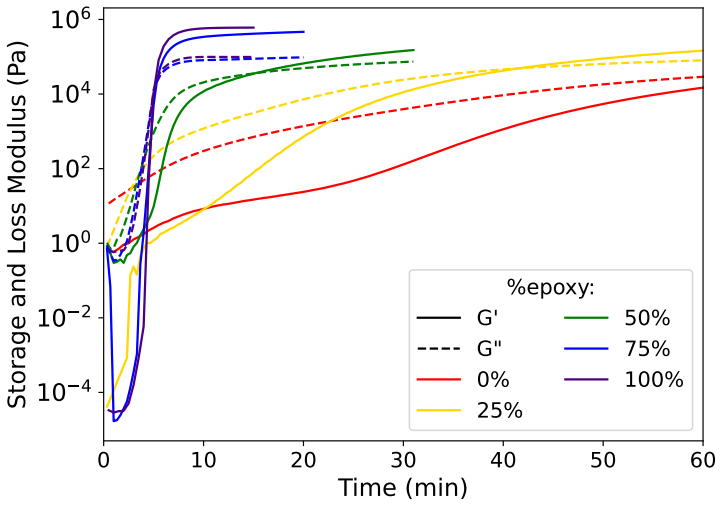

Figure S22: Curing rheological behavior at 80°C. Modulus evolution with time

V Influence of the hybridization on the mechanical properties of the neat resin

V.1 Results and discussion about the thermo-mechanical properties

First, the thermo-mechanical properties of the thermosets were assessed by DMA in tensile mode at different epoxy contents (Fig. S23c). Surprisingly, the hybrid materials' storage modulus was superior to pure epoxy or pure PHU thermosets. We demonstrated in a previous work the superior thermo-mechanical properties of PHU over a similar epoxy counterpart [5]. This was attributed to stronger H-bonds in PHU. In epoxides, the high crosslinking density plays a significant part in the mechanical properties in addition to the macromolecular backbone [6]. However, these permanent and strong covalent interactions lead to high stiffness and thermal stability but lower ductility. Herein, we do not observe any increase in the crosslinking density compared to PHU due to the use of only primary amine in the network. Yet, the PHU brings this strong and ductile H-bond ability. Importantly, the glass transitions are significantly increased compared to the pristine PHU, reaching values similar to the epoxy. This confirms the positive effect of the hybridization strategy through the engineering of the macromolecular structures bringing altogether different types of bonds (covalent and H-bonds) that interact together. As such, an increase in thermal stability and stiffness can be achieved while boosting toughness.

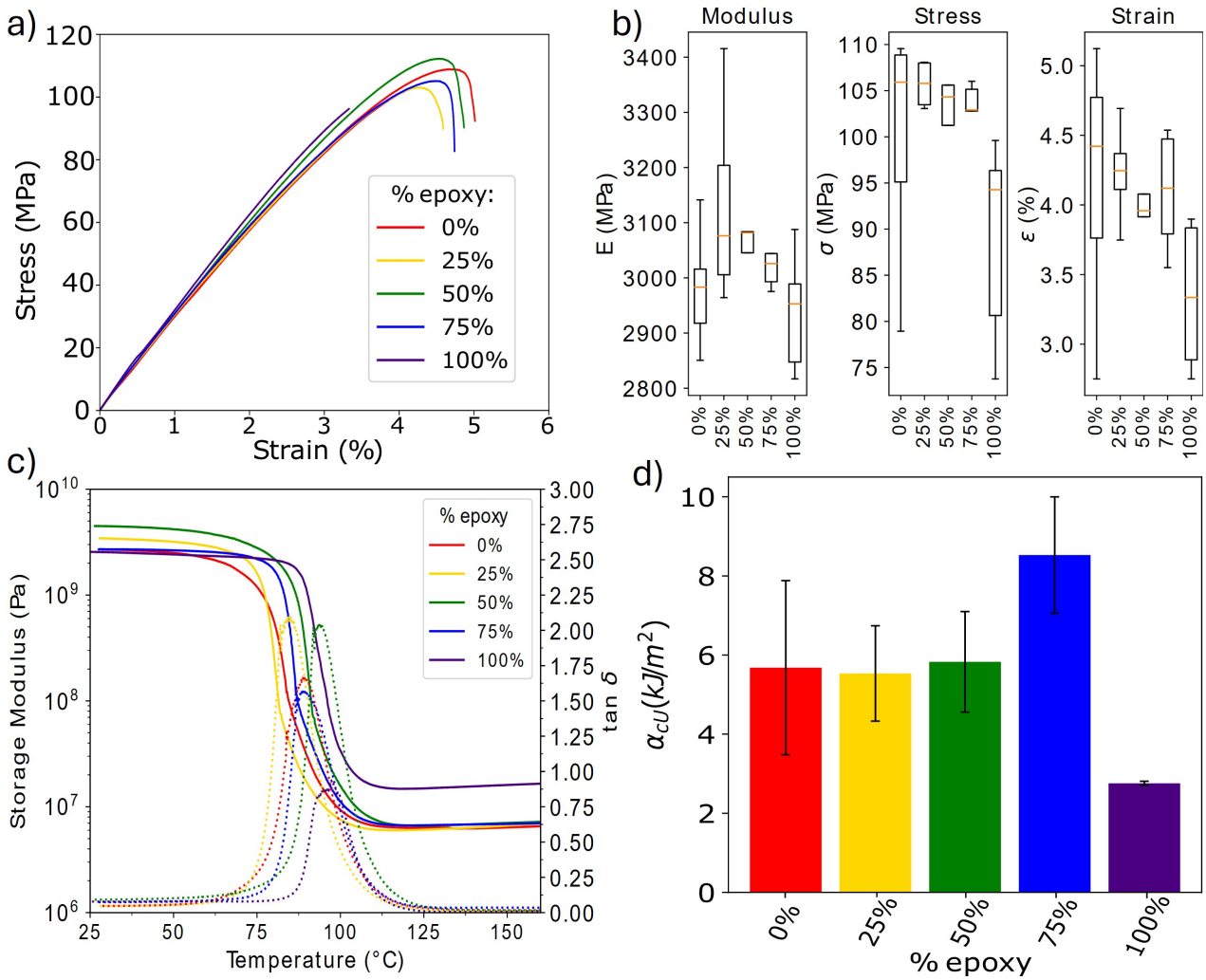

Figure S23: (thermo)Mechanical properties of the hybrid epoxy-PHU. a) Representative tensile strain-stress curves, b) boxplot of the tensile properties, c) DMA, and d) Charpy's impact results.

The quasi-static monotonic mechanical properties were assessed by tensile test (Fig. S23a-b), and extracted properties are summarized in the main manuscript. As already observed by DMA, a slight increase in Young's modulus was unveiled, highlighting the positive effect of this hybrid material on tuning the processability without decreasing the final properties. More importantly, in the realm of polymer, an increase in the modulus or glass transition may lead to a decrease in the ductility. This can be detrimental to the future structure's durability. In that hybridization strategy and as already evocated by DMA, the material incorporates "weak" H-bonds. This leads to equivalent or superior strain at break but also higher ultimate stress as the material possesses a better ability to absorb mechanical deformation with a higher stiffness [7].

This combined increase in the strain and stress is related to a higher work in the material, i.e. the toughness is increased. Therefore, the impact toughness of the material can be expected to increase in the hybrid material. For this reason, the impact toughness was evaluated through unnotched Charpy impact tests Fig. S23d. The results confirmed the observed trends with a positive hybridization effect on the toughness with similar toughness between pure PHU and hybrid and an increase close to 100% compared to the pure EP, in agreement with previous findings [8]. This is highly interesting as one of the issues about composite materials is their poor impact damage behavior, and is mainly driven by the matrix [9, 10]. In that sense, increasing the toughness of such structural materials through this simple hybrid process seems industrially relevant and greener than other processes such as the addition of modifiers and toughener that usually lead also to a decrease of other key-properties [11].

Yet, due to the close results, ANOVA was performed to better evaluate the modifications (see Fig.

S24). It reveals no significant statistical differences. Even if partly surprising, it remains a major result. Indeed, the primary objective was to substantially improve the processability and curing protocol, thus allowing implementation of PHU chemistry on a large scale. As the tensile results remain similar to pure EP or PHU, it discloses minor, although positive, modifications, that could simplify future implementation in industries as comparable to marketed EP systems. In impact toughness, only the hybrid containing 75% of EP was considered statistically different with an impact toughness of 8.5 kJ/mol, much higher than the pure EP (2.8 kJ/mol), other hybrids ranging in between EP and PHU.

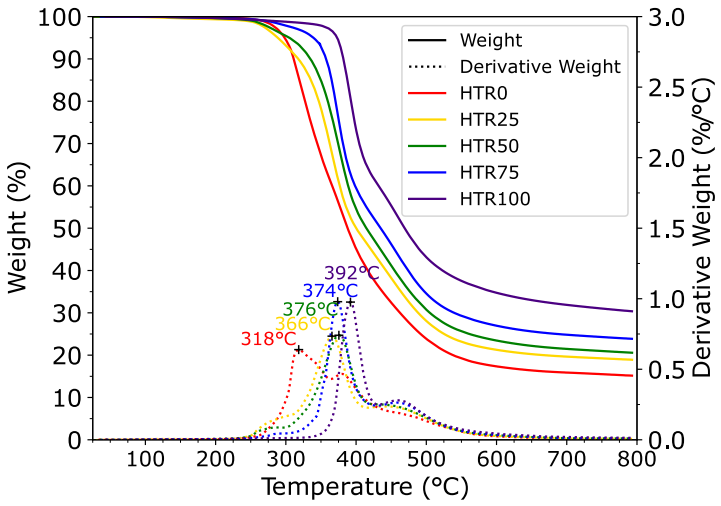

Figure S24: Thermal degradation under N_2 of the matrices

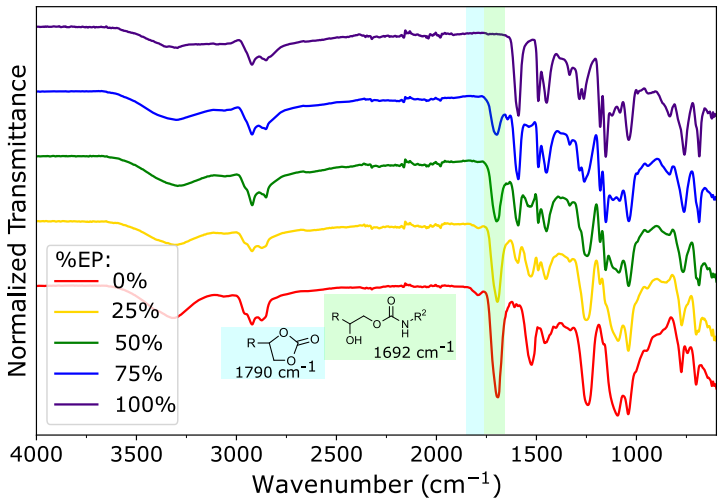

Figure S25: FTIR of the matrices.

V.2 ANOVA matrices

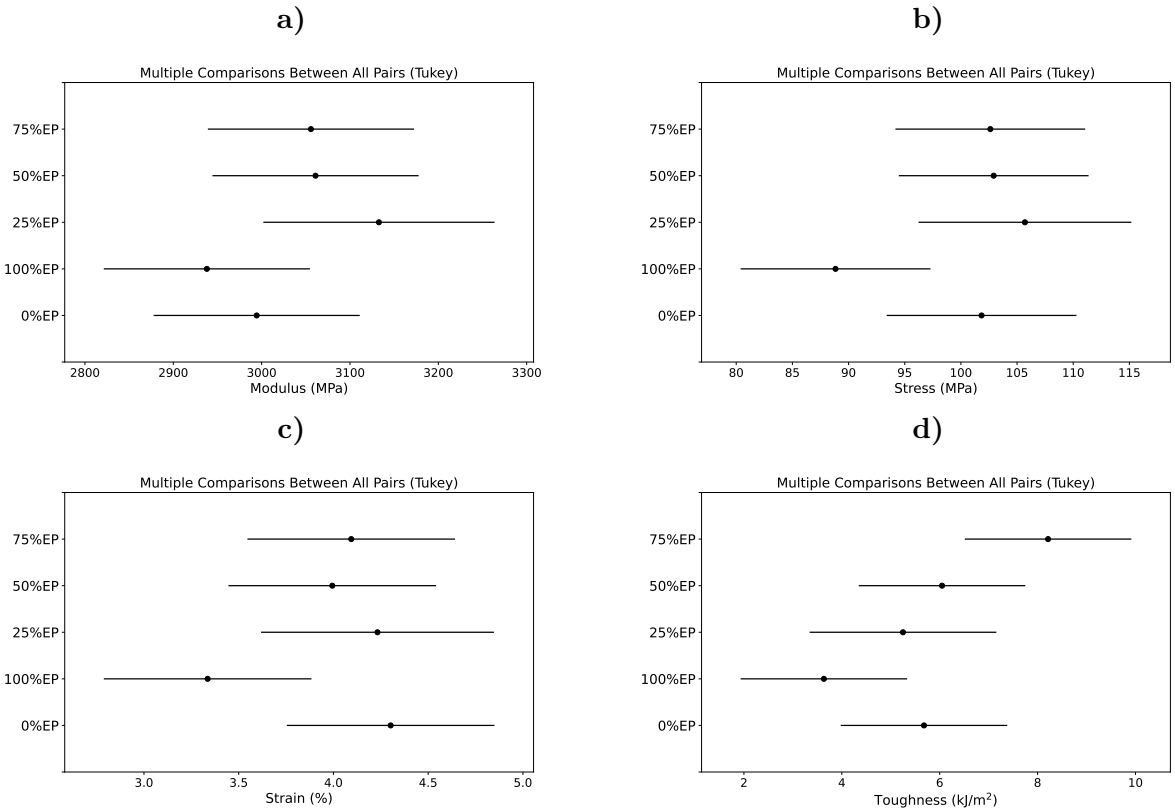

Figure S26: Tukey's Test results after ANOVA for the neat resin's mechanical properties a) Tensile Modulus, b) Stress at break, c) Strain at break, and d) Charpy's impact toughness.

VI RTM manufacturing of flax-EP-PHU composites

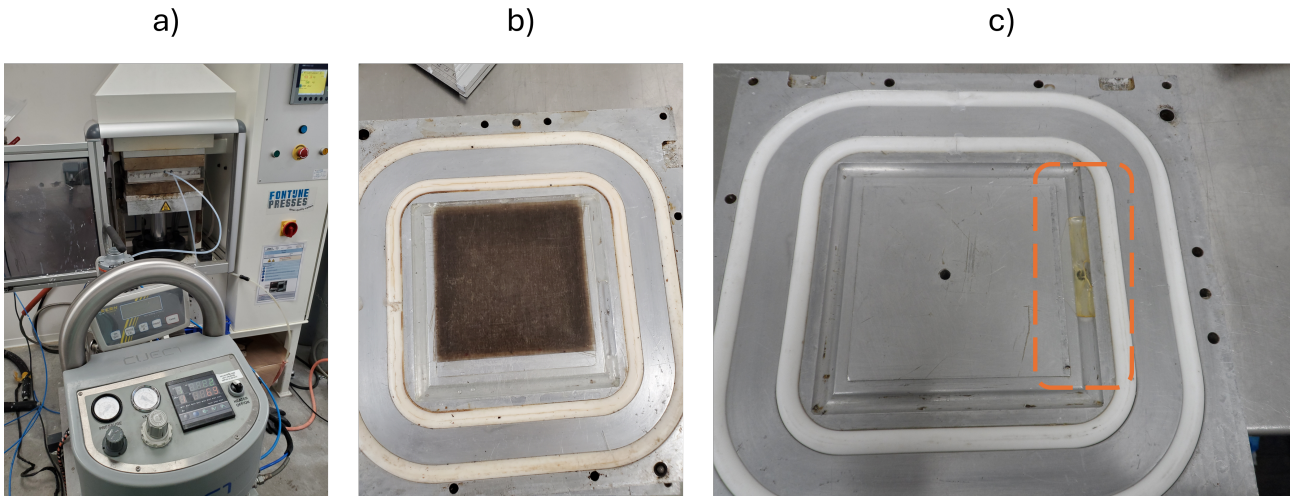

Figure S27: Resin Transfer Molding of Composites. a) RTM apparatus, b) Mold used with freshly made composite plate, and c) failed attempt to use 100% PHU as matrices for RTM injection.

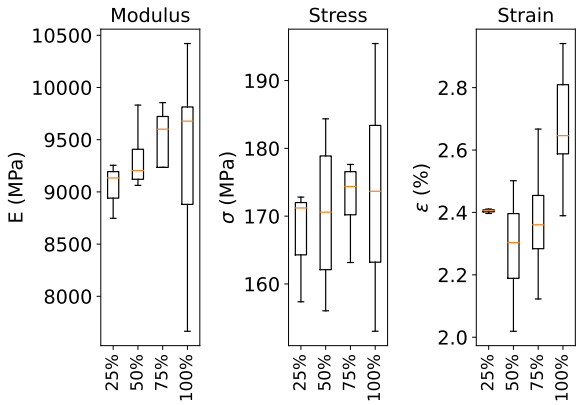

Figure S28: Boxplot of the bending properties in the transverse composite direction, corresponding to Fig.5c

VI.1 ANOVA Composites

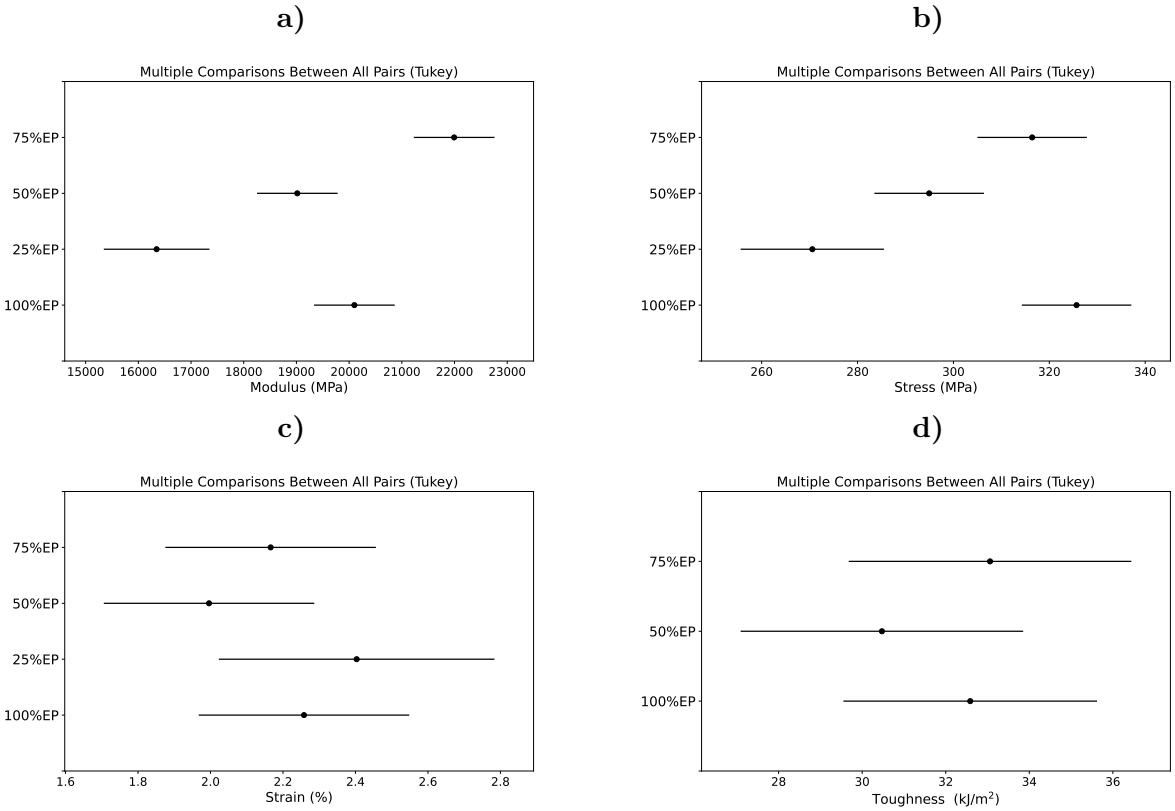

Figure S29: Tukey's Test results after ANOVA for the composite's mechanical properties in the principal fiber orientation. a) Tensile Modulus, b) stress at break, c) strain at break, and d) Charpy's impact toughness.

a)

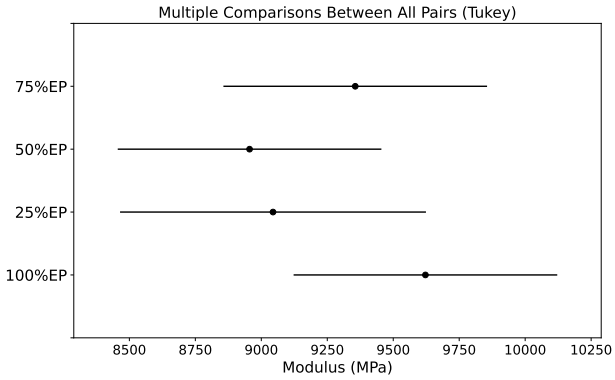

b)

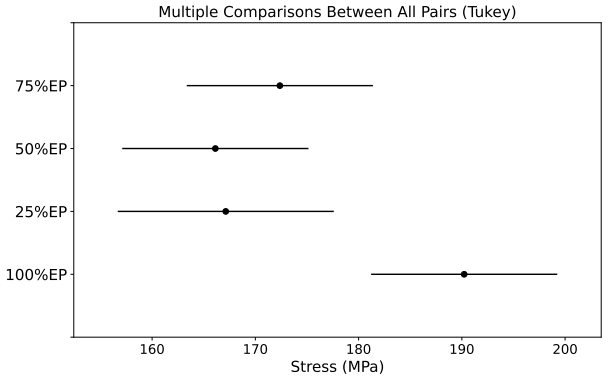

c)

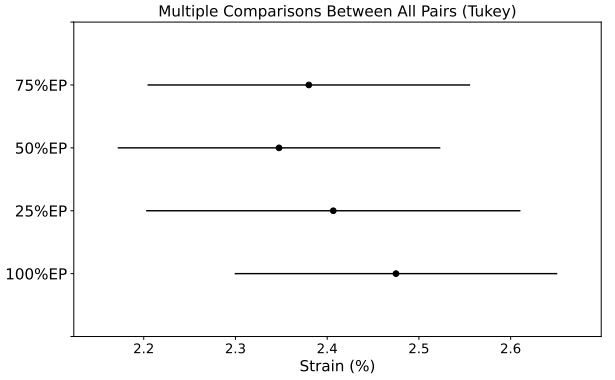

Figure S30: Tukey's Test results after ANOVA for the composite's mechanical properties in the transverse fiber orientation. a) Tensile Modulus, b) stress at break, c) strain at break.

VII Perspectives towards the reshaping and recycling of natural fiber composites

VII.1 Reshaping of composites

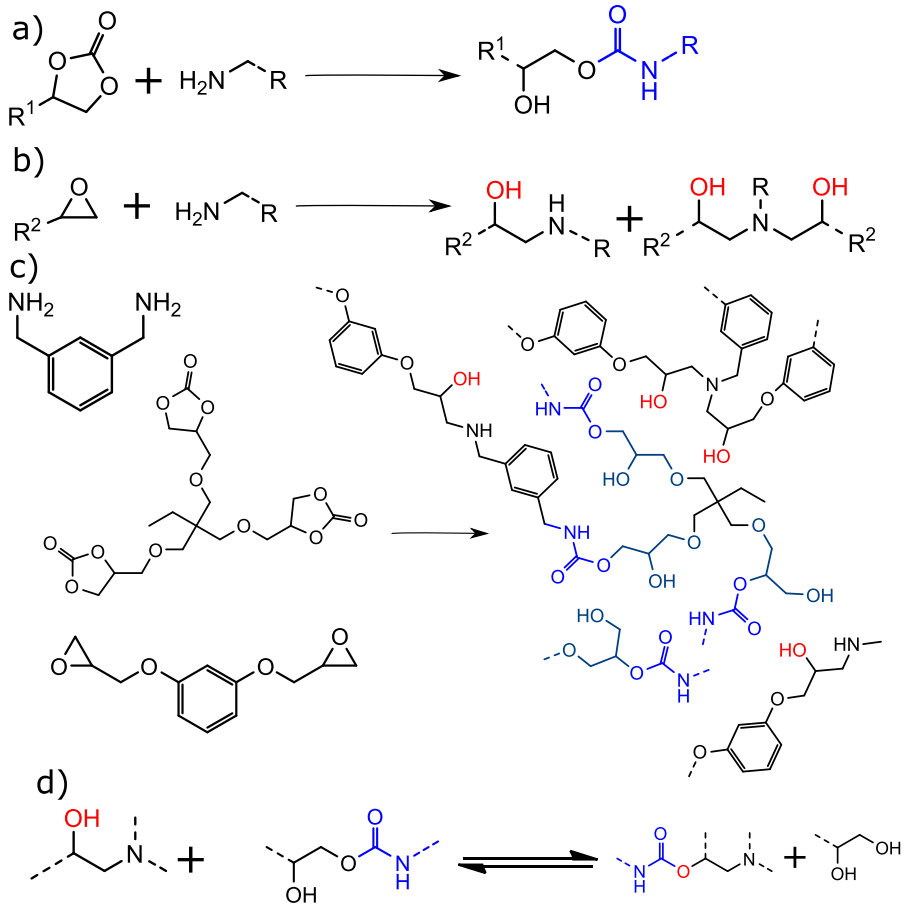

Figure S31: Representation of the synergetic hybrid EP-PHU network allowing the catalyst-free dynamicity. a) Aminolysis of cyclic carbonate into hydroxyurethane, b) Aminolysis of oxirane into amino-alcohols, c) representative structure of the formulated EP-PHU hybrid and d) catalyst-free exchange mechanism exploiting the amino-alcohols moieties and the hydroxyurethanes

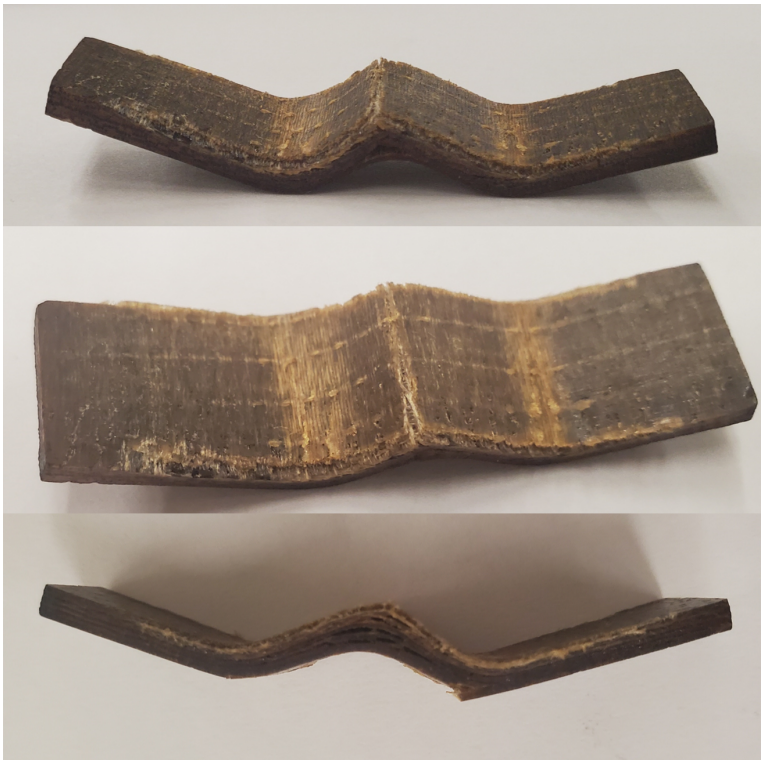

Figure S32: Attempting to reshape flax-epoxy composite

VII.2 TGA

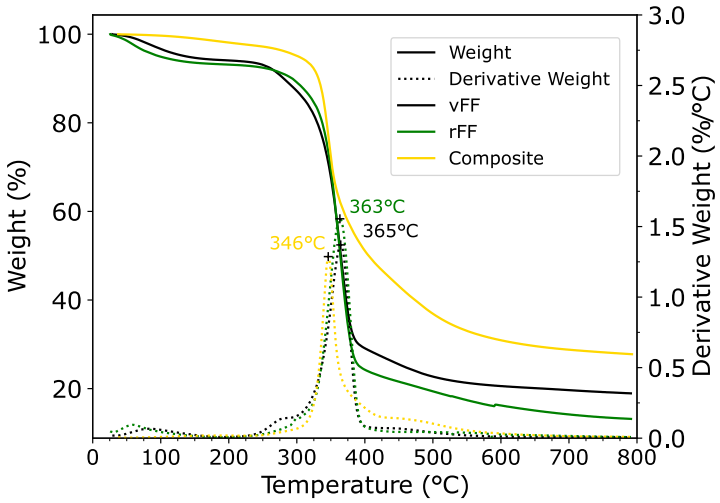

Figure S33: TGA of virgin fibers (vFF), reclaimed fibers (rFF) and the initial composite.

VII.3 SEM of virgin and recovered fibers

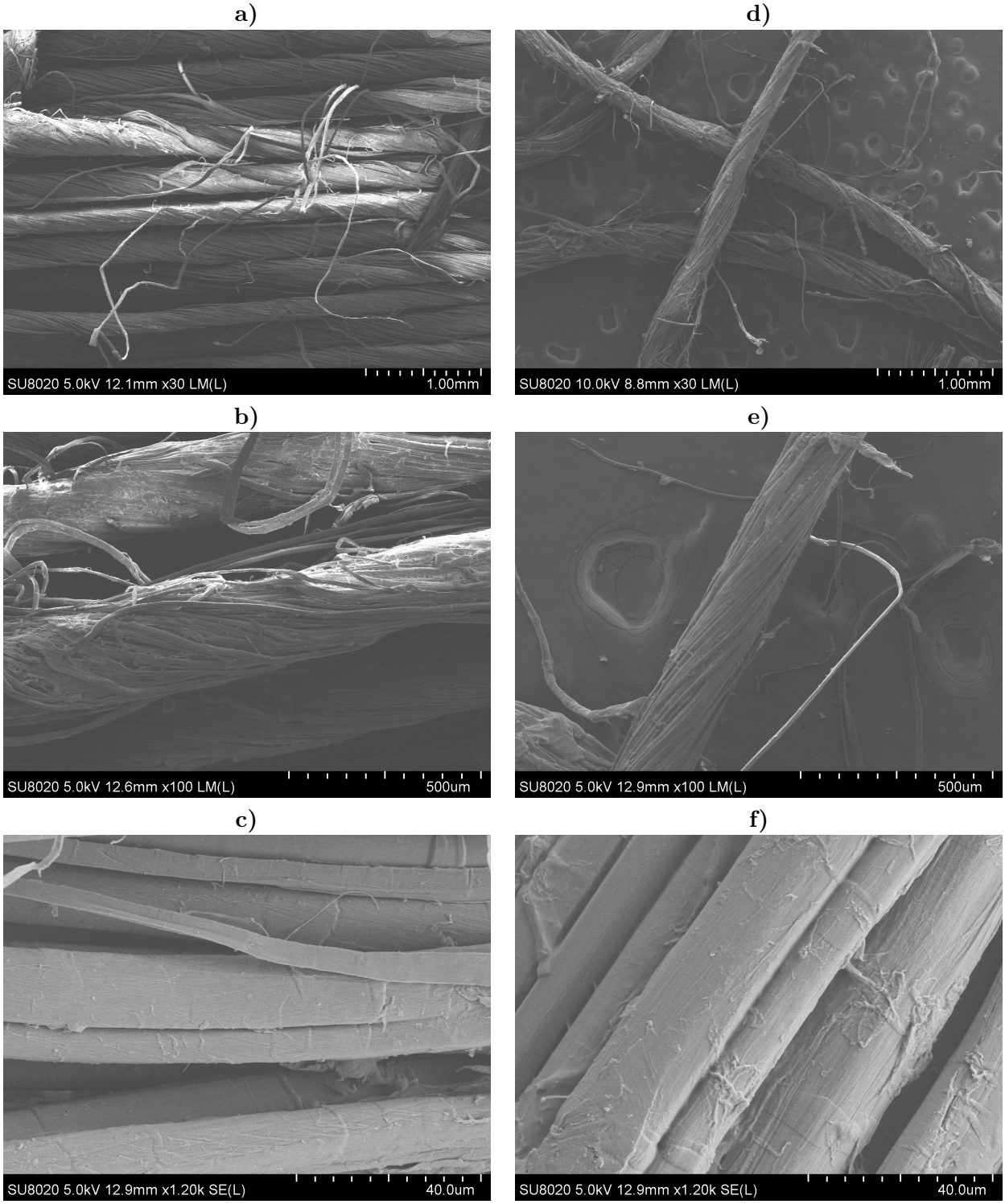

Figure S34: SEM images of a-c) virgin and d-f) recovered flax reinforcement. a,d) x30 magnifications, b,e) x100 magnifications, and c,f) x1200 magnifications.

VII.4 XPS

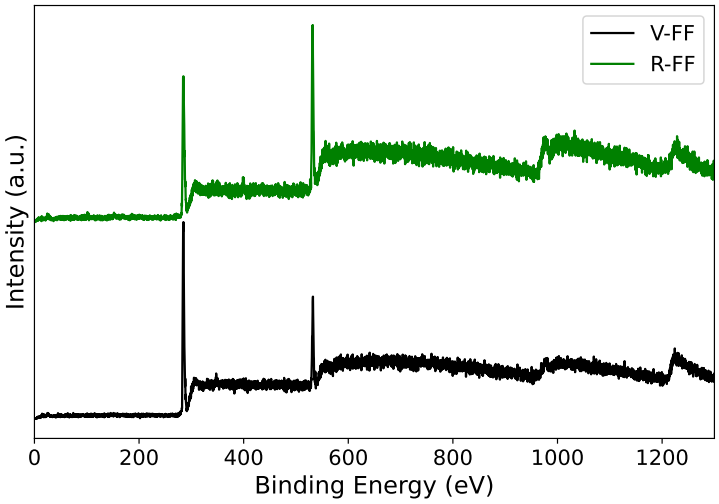

Figure S35: Composition survey of the virgin and recovered flax by XPS

Table S1: XPS results, surface composition for virgin flax fibers

Element	Name	Position	FWHM	Library RSF	Raw Area	Area/(RSF*T*MFP)	%At Conc	% Atomic rel
C	C-C, C-H	284.640	1.370	0.314	5103.400	707.590	56.97	81.93
	C-O	286.010	1.450	0.314	1551.430	215.050	17.31	
	C=O	287.460	1.540	0.314	484.770	67.180	5.41	
	O-C=O	288.690	1.620	0.314	201.010	27.850	2.24	
O	O1s	531.290	2.100	0.733	565.710	32.100	2.58	17.35
	O1s	532.620	2.100	0.733	3233.250	183.440	14.77	
Ca*	Ca (2p 3/2)	347.170	1.670	2.136	294.610	5.940	0.48	0.72
	Ca (2p 1/2)	350.780	1.670	2.136	147.310	2.970	0.24	

*Near noise spectrum, estimation

Table S2: XPS results, surface composition for reclaimed flax fibers

Element	Name	Position	FWHM	Library RSF	Raw Area	Area/(RSF*T*MFP)	%At Conc	% Atomic rel
C	C-C, C-H	284.610	1.480	0.314	1658.270	229.930	29.290	67.06
	C-N, C-O	286.090	1.480	0.314	1384.910	191.970	24.460	
	C=O?	287.450	1.480	0.314	538.860	74.680	9.510	
	N-C=O, O-C=O	288.840	1.570	0.314	215.480	29.850	3.800	
O	O1s	532.540	2.230	0.733	4078	231.370	29.470	29.47
N*	N1s	399.860	1.960	0.499	228.620	19.530	2.490	2.49
Si*	Si2p	101.960	2.080	0.429	73.070	7.670	0.980	0.98

*Near noise spectrum, estimation

VII.5 Energy-dispersive X-ray spectroscopy (EDX)

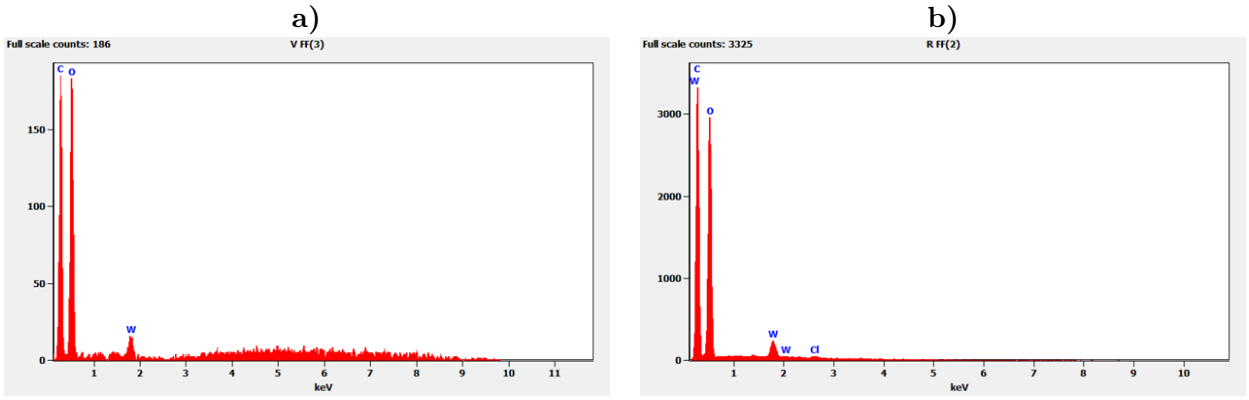

Figure S36: EDX of a) virgin fibers, and b) recovered flax fibers. The tungsten element (W) is due to the conductive coating for SEM observations and EDX analysis.

Table S3: Energy-dispersive X-ray spectroscopy (EDX) of virgin and recovered flax fibers

	V-FF		R-FF	
Element	Weight %	Atom %	Weight %	Atom %
C K	29.8 ± 0.6	36.1 ± 1.5	31.8 ± 0.2	38.5 ± 0.5
O K	70.2 ± 1.5	63.9 ± 2.8	66.9 ± 0.5	60.9 ± 0.8
Cl K	nd	nd	1.4 ± 0.2	0.6 ± 0.2
Total	100	100	100	100

VII.6 Tensile testing of the flax yarns

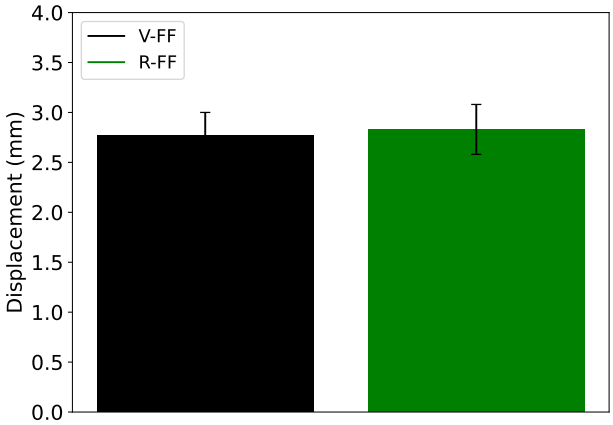

Figure S37: Admissible displacement of the virgin and recovered flax yarns.

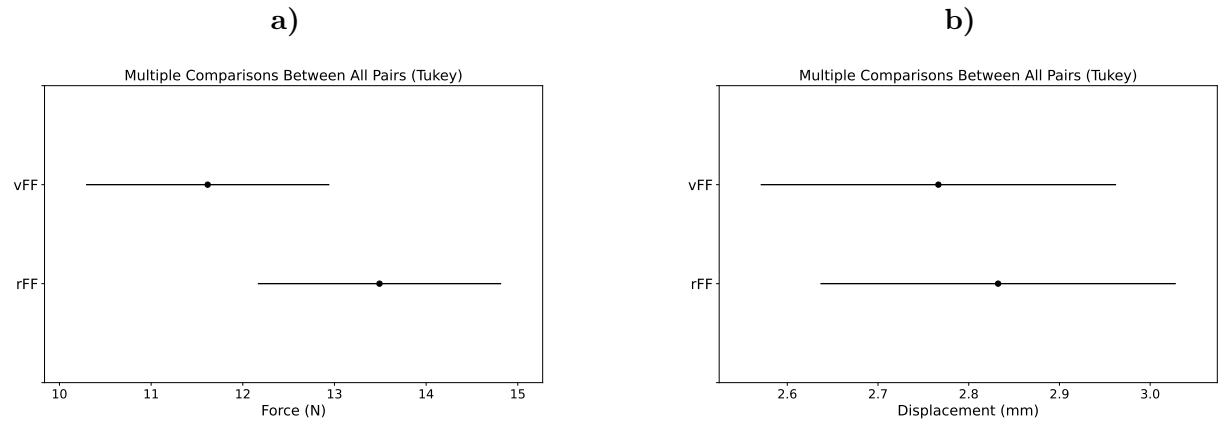

Figure S38: Tukey's Test results after ANOVA for the virgin and recovered flax yarns. a) Tensile strength, and b) Tensile elongation.

References

[1] Guillem Seychal, Connie Ocando, Leila Bonnaud, Julien De Winter, Bruno Grignard, Christophe Detrembleur, Haritz Sardon, Nora Aramburu, and Jean-Marie Raquez. Emerging Polyhydroxyurethanes as Sustainable Thermosets: A Structure–Property Relationship. *ACS Applied Polymer Materials*, 5(7):5567–5581, June 2023.

[2] Nihal Puhurcuoğlu and Yusuf Arman. Parameter estimation of epoxy resin cure kinetics by dynamics DSC data. *Polymers for Advanced Technologies*, 35(7):e6498, July 2024.

[3] Nichollas Guimarães Jaques, José William De Lima Souza, Matthias Popp, Jana Kolbe, Marcus Vinícius Lia Fook, and Renate Maria Ramos Wellen. Kinetic investigation of eggshell powders as biobased epoxy catalyzer. *Composites Part B: Engineering*, 183:107651, February 2020.

[4] Gp Sendeckyj, Ss Wang, W Steven Johnson, Ww Stinchcomb, and Cc Chamis. Mechanics of Composite Materials: Past, Present, and Future. *Journal of Composites Technology and Research*, 11(1):3, 1989.

[5] Guillem Seychal, Pierre Nickmilder, Vincent Lemaur, Connie Ocando, Bruno Grignard, Philippe Leclère, Christophe Detrembleur, Roberto Lazzaroni, Haritz Sardon, Nora Aranburu, and Jean-Marie Raquez. A novel approach to design structural natural fiber composites from sustainable CO 2 -derived polyhydroxyurethane thermosets with outstanding properties and circular features. *Composites Part A: Applied Science and Manufacturing*, 185:108311, October 2024.

[6] Ali Shokuhfar and Behrouz Arab. The effect of cross linking density on the mechanical properties and structure of the epoxy polymers: molecular dynamics simulation. *Journal of Molecular Modeling*, 19(9):3719–3731, September 2013.

[7] Jean-Emile Potaufeux, Jérémy Odent, Delphine Notta-Cuvier, Rémi Delille, Sophie Barrau, Emmanuel P. Giannelis, Franck Lauro, and Jean-Marie Raquez. Mechanistic insights on ultra-tough polylactide-based ionic nanocomposites. *Composites Science and Technology*, 191:108075, May 2020.

[8] R. Ghanbaralizadeh, H. Bouhendi, K. Kabiri, and M. Vafayan. A novel method for toughening epoxy resin through CO2 fixation reaction. *Journal of CO2 Utilization*, 16:225–235, December 2016.

[9] M. Dziendzikowski, A. Kurnyta, K. Dragan, S. Klysz, and A. Leski. In situ Barely Visible Impact Damage detection and localization for composite structures using surface mounted and embedded PZT transducers: A comparative study. *Mechanical Systems and Signal Processing*, 78:91–106, October 2016.

[10] Tulio Hallak Panzera, Thomas Jeannin, Xavier Gabrion, Vincent Placet, Chrystel Remillat, Ian Farrow, and Fabrizio Scarpa. Static, fatigue and impact behaviour of an autoclaved flax fibre reinforced composite for aerospace engineering. *Composites Part B: Engineering*, 197:108049, September 2020.

[11] Lidia Orduna, Iker Razquin, Itziar Otaegi, Nora Aranburu, and Gonzalo Guerrica-Echevarría. Ionic Liquid-Cured Epoxy/PCL Blends with Improved Toughness and Adhesive Properties. *Polymers*, 14(13):2679, June 2022.